Applied Ocean Research 114 (2021) 102771

Contents lists available at ScienceDirect

Applied Ocean Research

journal homepage: www.elsevier.com/locate/apor

Numerical simulations of liquid-solid flows with free surface by coupling IMPS and DEM

Fengze Xie [a], Weiwen Zhao [a], Decheng Wan [a,b,*]

[a] Computational Marine Hydrodynamics Lab (CMHL), School of Naval Architecture, Ocean and Civil Engineering, Shanghai Jiao Tong University, Shanghai 200240, China
[b] Ocean College, Zhejiang University, Zhoushan 316021, China

ARTICLE INFO

Keywords:
Liquid-solid flows
MPS method
DEM method
MPSDEM-SJTU solver

ABSTRACT

Liquid-solid two-phase flow with free surface is a significant issue in nature and engineering fields. In present study, an in-house solver MPSDEM-SJTU based on a fully Lagrangian coupled method is developed to solve the problems of liquid-solid two-phase flows. The improved moving particle semi-implicit (IMPS) method is applied for the simulation of incompressible viscous liquid flows while the discrete element method (DEM) is used to model the interaction among the solid particles. The coupling strategy is based on the local averaging technique. Multiple time-step algorithm is adopted for those two methods to balance the stability and the efficiency. The free surface detection and the solid-fluid neighbor search are modified. A simulation of multi-balls collapse is conducted to verify the DEM program of the present solver. The distributions of solid balls at different instants are in good agreement with the experimental results. Then, this solver is applied for two typical problems of two-phase flows, including the two-phase dam-break and the liquid-solid flows in a rotating cylindrical tank. The flow front, flow patterns and the shape of solid beds all agree well with experimental observations.

1. Introduction

Liquid-solid two-phase flows with free surface often occur in nature and engineering fields, such as sediment transport (Harada et al., 2019), debris flow (Hutter et al., 1996), separation in recycling processing (Markauskas et al., 2018), bead milling (Winardi et al., 2018) and etc. This phenomenon is very complicated. In addition to the contact force, solid particles are acted upon by hydrodynamics, while the distributions of pressure and velocity in the fluid field are affected by solid particles.

Although model experiments are more reliable, it is time consuming and limited by space. Besides, it is difficult to capture detailed flow field information. In recent years, many numerical meshless methods, e.g. Smoothed Particle Hydrodynamics method (SPH; Gingold and Monaghan (Gingold and Monaghan, 1977)), Imcompressible SPH (ISPH; Shao and Lo (Shao and Lo, 2003)), Moving Particle Semi-implicit method (MPS; Koshizuka et al. (Koshizuka et al., 1995)) and Discrete Element Method (DEM; Cundall and Strack (Cundall and Strack, 1979)) have been applied to the nature and engineering field (Gotoh and Khayyer, 2018), including Fluid-Structure Interaction (FSI) (Zhang et al., 2020, Zhu et al., 2021, Khayyer et al., 2018), multiphase flows (Shimizu et al., 2020), fluid flows passing through porous media (Tsurudome et al., 2020) and etc. In the problems of liquid-solid flows, it is more suitable for particle methods to handle the large deformation of not only the free surface but also the interface. Tsuruta et al. (Tsuruta et al., 2019) used the PARISPHERE code based on the ISPH and DEM to solve a series of coastal engineering problems, including the dam-break flows interacting with porous media and overflowing tsunami scouring the sediment of sands. Ikari et al. (Ikari et al., 2020) employed SPH to investigate the diffusion of the dumped sand in the fluid and the deposition of the sand was considered. Tajnesaie et al. (Tajnesaie et al., 2018) simulated the submerged landslide with Weakly Compressible MPS (WCMPS).

For the methods mentioned above, the solid phase of the two-phase flows is treated as the continuum (Khanpour et al., 2016) or discrete particles (Feng and Yu, 2004). Considering the computational cost, the former is more suitable for the large-scale problems. Xiong et al. (Xiong et al., 2011) proposed a Smoothed Particle Hydrodynamics (SPH) method based on Two Fluid Model (TFM) for the particle-fluid fluidizations. The fluid phase and solid phase were solved separately. The solid-solid interaction was described by stress tension and only one inter-phase force-drag force is considered. Jandaghian et al. (Tajnesaie et al., 2021) developed an Enhanced Weakly-Compressible MPS

* Corresponding author.
E-mail address: dcwan@sjtu.edu.cn (D. Wan).

https://doi.org/10.1016/j.apor.2021.102771
Received 10 April 2021; Received in revised form 25 June 2021; Accepted 26 June 2021

(EWMPS) with a unified rheological model to simulate the submerged landslides. The solid and fluid phase were solved in one framework. The particles of different phase could not overlap with each other and they were always modelled with the same size. The solid part was regarded as the mixture of solid and fluid. Its density and viscosity were determined by the volume fraction of the solid.

Although the methods with solid being continuum are time saving, some important information is neglected, such as the forces acting on and motion behaviors of a single particle. In the contrast, the discrete method emphasizes the interactions among solid particles and the simulation is more realistic. The Discrete Element Method (DEM) is a Lagrangian method for solid phase, which is based on the Newton's second law and widely used in simulations of granular flows, e.g., landsides (Tan and Chen, 2017), powder mixing (Pantaleev et al., 2017) and the discharge flow in silos (González-Montellano et al., 2011). In recent years, an amount of coupling methods of DEM and other particle methods have been developed for the simulation of liquid-solid flows with free surface. The solid DEM particles can be treated as the float bodies directly (Zhang et al., 2009) and their boundaries needs to be modelled by many fine particles, which makes the number of fluid particles in the computational domain increase largely and leads to a heavy computational load. Another coupling scheme was proposed based on the local average technique (Anderson and Jackson, 1969). Robinson et al. (Robinson et al., 2014) developed a SPH-DEM method and simulated the sediment of single particle, block with constant porosity and multi particles. The effect of fluid resolution, drag laws, fluid properties and local volume fraction of fluid to the simulation results were also discussed in detail. Tan and Chen (Tan and Chen, 2017) coupled DEM with an improved SPH method ($\delta-$ SPH), which was proved to avoid pressure oscillation effectively. The evolution process of the surge wave generated by landslide was studied. Sun and Sakia (Sun et al., 2014, Sun et al., 2013) combined DEM with WCMPS and SPH, respectively. A series of experiments such as liquid-solid flows in a rotating cylindrical tank and liquid-solid dam-break were carried out to verify the accuracy and stability of those solvers. He et al. (He et al., 2018) proposed an efficient neighbor search algorithm with the help of background grids and introduced the GPU acceleration technique to SPH-DEM, which highly improved the computation efficiency. Based on the work mentioned above, the coupling methods of weakly compressible particle methods (e.g., SPH, WCMPS) and DEM have been widely applied in different fields. For example, Iwamoto et al. (Iwamoto et al., 2019) investigated the interaction between the tsunami and the breakwater. The numerical model of the breakwater was composed of DEM particles with the bonds. Markauskas et al. (Markauskas and Kruggel-Emden, 2019) introduced the resistance force to the SPH-DEM model and analyzed the process of wet continuous screen. Li el al. (Li et al., 2019) applied WCMPS-DEM to the simulation of non-Newtonian liquid-solid flows and discussed the influence of the radius particles interaction to the numerical results. Xu and Dong (Xu and Dong, 2021) simulated the 3-D large-scale landslide-induced tsunamis by SPH-DEM with GPU acceleration technique.

The researches on the coupling of projection-based particle method and DEM were relatively small. Sakia (Sakai et al., 2012) coupled DEM with original MPS and investigated the influences of different hydrodynamic forces on the movements of the solid particles. Harada et al. (Harada et al., 2019) used MPS-DEM to simulate the process of swash beach. The local volume fraction only considered in the calculation of drag force. If the local volume fraction is added to the Pressure Poisson Equation (PPE) and the gradient model of the original impressible MPS method, the MPS-DEM coupling method may not be robust and stable enough. In the past several years, researchers have done much work (Luo et al., 2021) to enhance the stability and accuracy of projection-based particle methods (e.g., ISPH, MPS). Tanaka and Masunaga (Tanaka and Masunaga, 2010) developed a gradient model of momentum conservation and a mixed source term of Pressure Poisson Equation (PPE) to make the pressure field smooth in terms of both time and space. Khayyer et al. (Khayyer and Gotoh, 2010, Khayyer and Gotoh, 2012, Khayyer and Gotoh, 2011, Khayyer and Gotoh, 2009) proposed several high-order schemes for Laplacian model, gradient model and source term of PPE, which could successfully reduce unphysical pressure fluctuation. Based on those modified models, projection-based particle methods were applied for more complicated problems, including Fluid-Structure Interaction (FSI) (Khayyer et al., 2018, Khayyer et al., 2018, Khayyer et al., 2021, Khayyer et al., 2021), liquid-solid flows (Harada et al., 2019), multi-phase flows (Khayyer et al., 2019) and etc. Wang et al. (Wang et al., 2019) further proposed a Back Mesh (BM) method to improve the continuity of the source term of PPE and the pressure calculation was enhanced. In present work, the improved MPS (IMPS) with gradient model of momentum conservation and mixed source term of PPE, whose stability and accuracy has been verified in (Zhang and Wan, 2017), is coupled with DEM.

In this paper, an in-house solver MPSDEM-SJTU based on the coupling method of IMPS and DEM is developed for the simulations of liquid-solid flows. The free surface detection and the solid-fluid neighbor search are modified. A multiple time-step strategy, which is often used in FSI solver, is introduced to present solver. In the first section, an improved MPS method, a DEM method and their coupling algorithm are presented briefly. In the second section, the benchmark case, multilayer ball collapse is conducted and compared with the experimental and other numerical results to verify the accuracy of new developed DEM solver. Then, two numerical simulations, are carried out by the MPSDEM-SJTU solver. In the first example of two-phase dam-break, numerical results by MPS-DEM and IMPS-DEM model in settling process are compared to confirm the stability of the latter. Numerical results with different MPS resolutions are compared with experimental data to check the convergency and accuracy of IMPS-DEM model. The necessity of the new solid-fluid search strategy is also investigated. Besides, the evolution of solid-fluid flows is discussed. The second case of two-phase flow in a rotating cylindrical tank is simulated to show the performance of present solver with moving boundary.

2. Numerical methods

2.1. Liquid phase

The local average technique established by Anderson and Jackson (Anderson and Jackson, 1969) is used to balance the exchange of momentum. There are two typical forms of the fluid momentum equations, model A and Model B (Kafui et al., 2002). Model B is adopted in this solver, which assumes that the pressure drop applied to fluid phase only (Feng and Yu, 2004).

$$\frac{\partial}{\partial t}\left(\widetilde{\rho}_f\right)+\nabla\cdot\left(\widetilde{\rho}_f\vec{u}\right)=0 \tag{1}$$

$$\frac{D}{Dt}\left(\widetilde{\rho}_f\vec{u}\right)=-\nabla p+\varepsilon_f\mu_f\nabla^2\vec{u}+\widetilde{\rho}_f\vec{g}-\vec{f}^{\,\mathrm{int}} \tag{2}$$

$$\widetilde{\rho}_f=\varepsilon_f\rho_f \tag{3}$$

where subscript f denotes the fluid particle. ε_f, ρ_f, $\vec{u}_f$, p, μ_f, $\vec{g}$ and t denote the local volume fraction, the fluid density, the velocity vector of fluid, the pressure, the dynamic viscosity, the gravity acceleration vector and the physical time, respectively. $\vec{f}^{\,\mathrm{int}}$ denotes the body force due to the momentum exchange between solid phase and liquid phase.

In MPS method, the interaction between particles is controlled by kernel function $W(r)$, which plays a role of weight function in the discretization process. In order to avoid non-physical pressure oscillation, the kernel function presented by Zhang et al. (Zhang et al., 2014) is employed here.

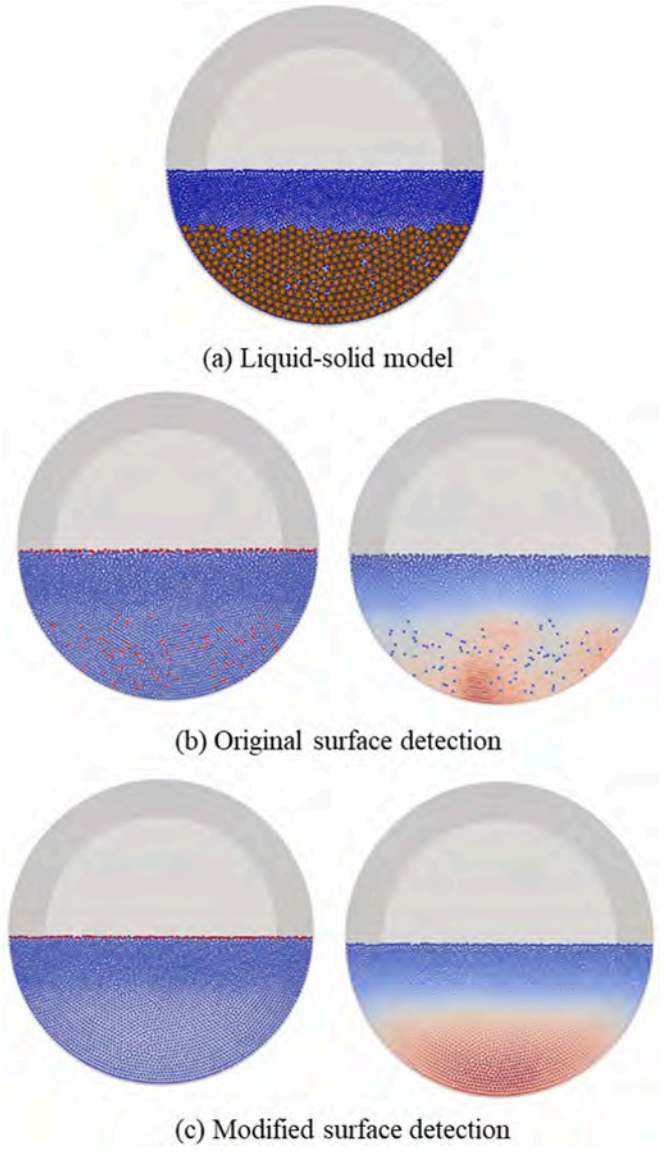

Fig. 1. Comparison of the numerical results obtained by the IMPS-DEM with the original free-surface detection and the IMPS-DEM with the modified free-surface detection (Left: red dots represent the detected surface particles. Right: pressure field).

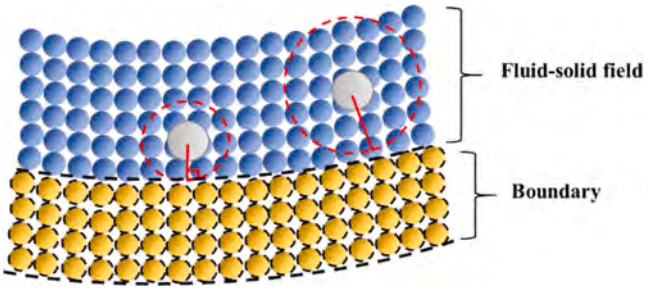

Fig. 2. Neighbor search strategy for solid-fluid particles near the solid boundaries.

$$W(r)=\begin{cases}\dfrac{r_e}{0.85r+0.15r_e}-1 & 0\le r<r_e\\ 0 & r_e\le r\end{cases} \tag{4}$$

where r denotes the distance between two particles and r_e denotes the radius of particles interaction. r_e is set to $2.1r_0$ for the gradient model and the number density. r_e is set to $6.01r_0$ for the Laplacian model and the two-phase interaction model. r_0 is the initial particle spacing.

The number density reflects the distribution of fluid particles, which is directly proportional to the density of the fluid, given by,

$$<n>_i=\sum_{j\neq i}W\left(\left|\vec{r}_j-\vec{r}_i\right|\right) \tag{5}$$

where subscripts i and j denote the fluid particles, and $\vec{r}$ is the position vector relative to origin. For simulation of single-phase incompressible fluid, the particle number density is required to be consistent with initial particle number density n_0. To solve the problem of mixture solid-fluid flows, the local volume fraction should be considered and the particle number density should be kept at a constant value (Sakai et al., 2012).

$$<n>_i=\varepsilon_i n^0=\widetilde{n}^0 \tag{6}$$

The n_0 in particle interaction models is simply taken place by the $\widetilde{n}^0$. The particle interaction models include gradient model (Tanaka and Masunaga, 2010), divergence model and Laplacian model (Koshizuka et al., 1995).

$$<\nabla\phi>_i=\frac{d}{\widetilde{n}^0}\sum_{j\neq i}\frac{\phi_j+\phi_i}{\left|\vec{r}_j-\vec{r}_i\right|^2}\left(\vec{r}_j-\vec{r}_i\right)\cdot W\left(\left|\vec{r}_j-\vec{r}_i\right|\right) \tag{7}$$

$$\langle\nabla\cdot\vec{u}\rangle_i=\frac{d}{\widetilde{n}^0}\sum_{j\neq i}\frac{\left(\vec{r}_j-\vec{r}_i\right)\cdot\left(\vec{u}_j-\vec{u}_i\right)}{\left|\vec{r}_j-\vec{r}_i\right|^2}W\left(\left|\vec{r}_j-\vec{r}_i\right|\right) \tag{8}$$

$$<\nabla^2\phi>_i=\frac{2d}{\widetilde{n}^0\lambda}\sum_{j\neq i}(\phi_j-\phi_i)\cdot W\left(\left|\vec{r}_j-\vec{r}_i\right|\right) \tag{9}$$

$$\lambda=\frac{\sum_{j\neq i}W\left(\left|\vec{r}_j-\vec{r}_i\right|\right)\cdot\left|\vec{r}_j-\vec{r}_i\right|^2}{\sum_{j\neq i}W\left(\left|\vec{r}_j-\vec{r}_i\right|\right)} \tag{10}$$

where ϕ denotes the physical quantity carried by the MPS particles, d is the number of space dimensions, λ is a parameter which is used to make the variance increase equal to the analytical solution (Koshizuka et al., 1995).

The pressure of the flow field is obtained by solving the pressure Poisson equation (PPE). Mixed source term method (Tanaka and Masunaga, 2010, Khayyer and Gotoh, 2011) is used to solve PPE, given by,

$$\nabla^2 p_i^{m+1}=(1-\gamma)\frac{\rho_f}{\Delta t}\nabla\cdot\vec{u}_i^*-\gamma\frac{\rho_f}{\Delta t^2}\frac{<n^*>_i-\widetilde{n}^0}{n^0} \tag{11}$$

where p_i^{m+1} denotes the pressure at the step of $m+1$, γ denotes a blending parameter varying from 0 to 1, Δt denotes the time step, $\vec{u}_i^*$ and $<n^*>_i$ are the intermediate velocity and the intermediate particle density. In this paper, the value of γ is set to 0.001.

A free surface detection method Zhang et al., 2014) based on the asymmetry distribution of neighboring particles, whose basic concept is similar to the method in (Khayyer et al., 2009), is adopted here, as shown in Eqs (12)-((14). This method can distinguish the particles of free surface from the others more accurately with a slight increase in computational cost. In the incompressible MPS method, the characteristic of incompressibility of fluid is satisfied by keeping the particle density at every time step consistent with the initial particle density $\widetilde{n}^0$, which can be founded in the second term of Eq. (11). The $\widetilde{n}^0$ is equal to

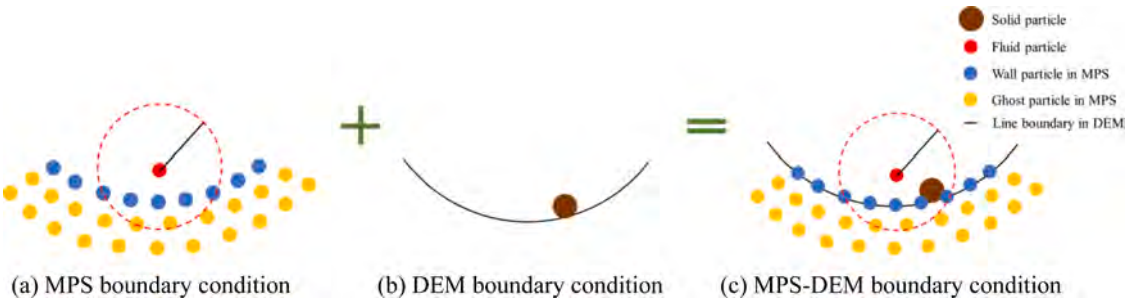

Fig. 3. The conceptual illustration of MPS-DEM coupling boundary condition.

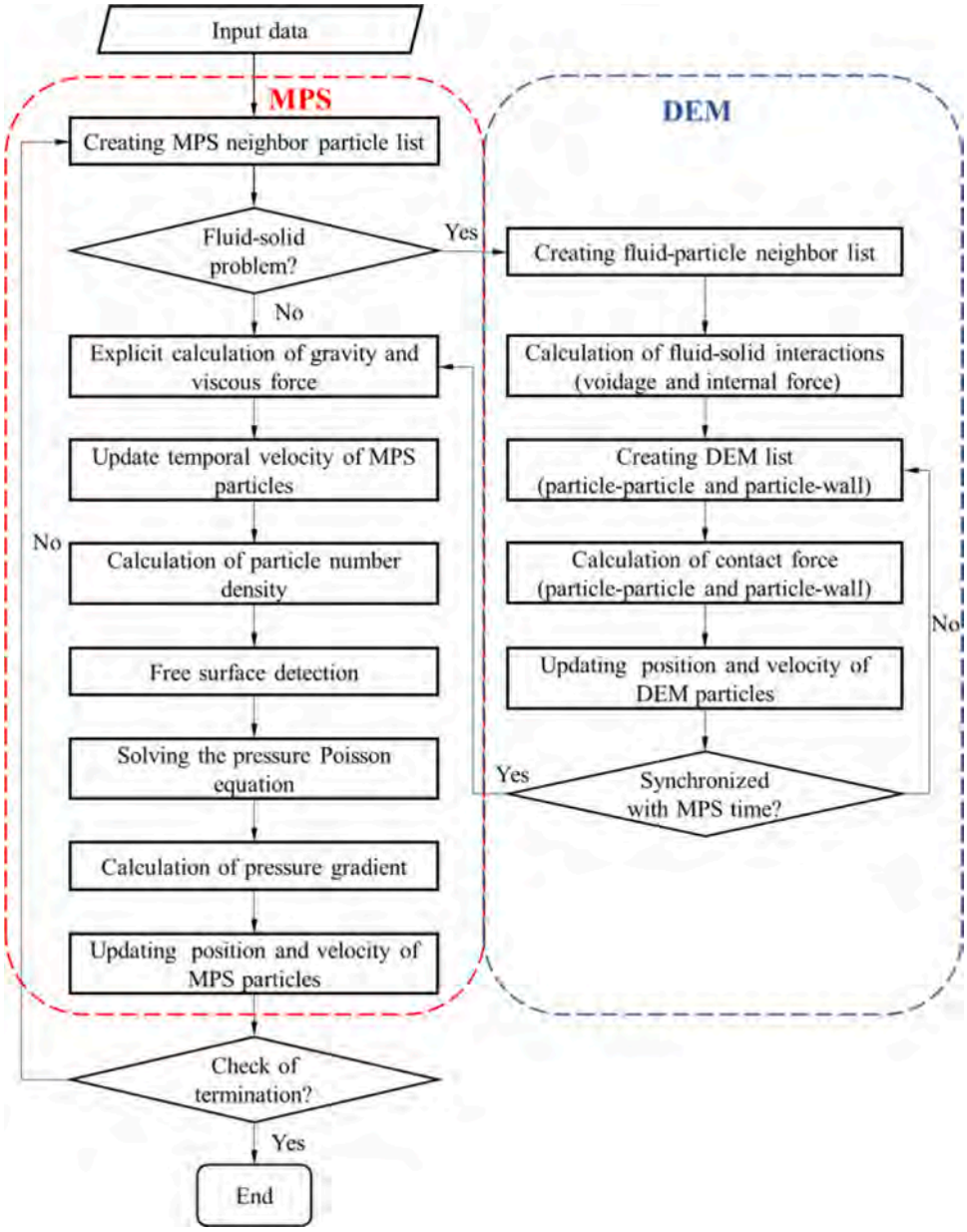

Fig. 4. Flow chart of coupling strategy between MPS and DEM.

$\varepsilon_i n^0$. ε_i is the local volume fraction, which varies according to the aggregation of the solid particles in the fluid field. Due to the existence of DEM particles, the ε_i is less than 1. Therefore, the spacing of the fluid particles near the DEM particles should be larger than those far away from the DEM particles and those inner fluid particles may be wrongly regarded as particles of the free surface, which will influence the accuracy and stability of the simulation. Based on the free surface detection method, the modified free surface detection method is proposed as

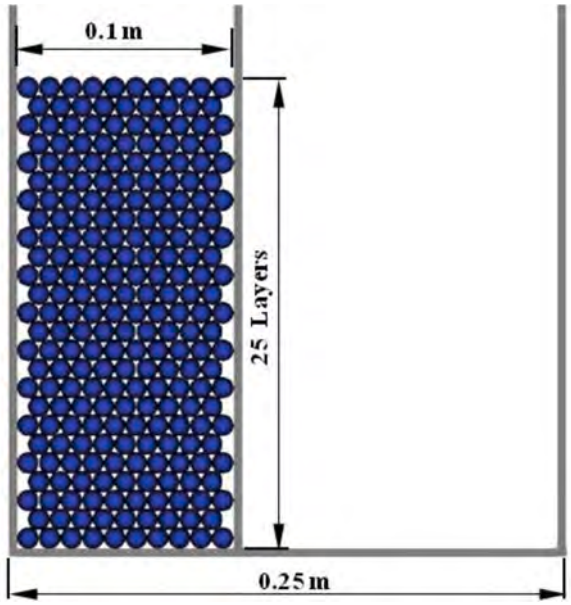

Fig. 5. Balls' distribution at $t = 0$s - multilayer balls collapse.

Table 1
DEM parameters in the simulation of multilayer balls collapse.

Parameters of the balls	Values	Parameters of the Walls	Values
Density (kg /m^3)	7930	Young's modulus (N/m^2)	30×10^8
Diameter (m)	0.01	Poisson's ratio	0.3
Young's modulus (N /m^2)	2×10^{11}	Static friction coefficient	0.3
Poisson's ratio	0.3	Rolling friction coefficient	0.15
Static friction coefficient	0.35	Coefficient of restitution	0.7
Rolling friction coefficient	0.15	-	-
Coefficient of restitution	0.7	-	-

shown in Eqs (15)-(17). The n_0 is simply replaced by $\tilde{n}^0$. Fig. 1 shows the comparison of the free surface detection between the original method (n^0) and the modified method ($\tilde{n}^0$). The pressure field is smoother and the detection of free surface is more accurate in the simulation with modified free surface detection.

$$< n >_i^* < \beta n^0 \tag{12}$$

$$< \vec{F} >_i = \frac{d}{n^0}\sum_{j\neq i}\frac{1}{\left|\vec{r}_i - \vec{r}_j\right|}\left(\vec{r}_i - \vec{r}_j\right)W\left(\left|\vec{r}_j - \vec{r}_i\right|\right) \tag{13}$$

$$< \left|\vec{F}\right| >_i > \alpha\left|\vec{F}_0\right| \tag{14}$$

$$< n >_i^* < \beta\tilde{n}^0 \tag{15}$$

$$< \vec{F} >_i = \frac{d}{\tilde{n}^0}\sum_{j\neq i}\frac{1}{\left|\vec{r}_i - \vec{r}_j\right|}\left(\vec{r}_i - \vec{r}_j\right)W\left(\left|\vec{r}_j - \vec{r}_i\right|\right) \tag{16}$$

$$< \left|\vec{F}\right| >_i > \alpha\left|\vec{F}_0\right| \tag{17}$$

2.2. Solid phase

The motion of solid particles is simulated based on DEM method (Cundall and Strack, 1979) which is governed by Newton's second law, expressed as,

$$m_k\frac{D\vec{v}_k}{Dt} = \sum_l \vec{F}_{c,\,kl} + m_k\vec{g} + \vec{F}_k^{\,\mathrm{int}} \tag{18}$$

$$I_k\frac{D\vec{\omega}_k}{Dt} = \sum_l \vec{T}_{c,\,kl} \tag{19}$$

where the subscripts k and l denote solid particles. m_k, I_k, $\vec{v}_k$ and $\vec{\omega}_k$ denote, the mass, the moment of inertia, the translational and rotational velocities of DEM particle k, respectively. $\vec{F}_{c,\,kl}$ and $\vec{T}_{c,\,kl}$ denote the contact force and moment due to the solid-solid interaction, respectively. $\vec{F}_k^{\,\mathrm{int}}$ denotes the hydrodynamic force applied to the DEM particles.

The DEM particles are treated as soft spheres and they are allowed to overlap to each other. The Hertz-Mindlin model (Hertz, 1881, Mindlin, 1949) is selected as the collision model in this work. The contact model consists of dashpots, springs and sliders. The contact force $\vec{F}_{c,\,kl}$ can be decomposed into the normal and tangential components and both components consist of elastic force and damping force. The elastic forces $\vec{F}_{e,\,kl}^{\,n}$ and $\vec{F}_{e,\,kl}^{\,t}$are given by,

$$\vec{F}_{e,\,kl}^{\,n} = -\frac{4}{3}E^*\sqrt{R^*\left|\vec{\delta}_{kl}^{\,n}\right|}\vec{\delta}_{kl}^{\,n} \tag{20}$$

$$\vec{F}_{e,\,kl}^{\,t} = -8G^*\sqrt{R^*\left|\vec{\delta}_{kl}^{\,n}\right|}\vec{\delta}_{kl}^{\,t} \tag{21}$$

where $\vec{\delta}_{kl}^{\,n}$ and $\vec{\delta}_{kl}^{\,t}$ denote the relative displacement in normal and tangential direction between particle k and particle l. E^*, R^* and G^* denote the equivalent Young's modulus, equivalent radius and equivalent shear modulus of two particles in contact, respectively, defined by,

$$\frac{1}{E^*} = \frac{1-\nu_k^2}{E_k} + \frac{1-\nu_l^2}{E_l} \tag{22}$$

$$\frac{1}{R^*} = \frac{1}{R_k} + \frac{1}{R_l} \tag{23}$$

$$\frac{1}{G^*} = \frac{2(2-\nu_k)(1+\nu_k)}{E_k} + \frac{2(2-\nu_l)(1+\nu_l)}{E_l} \tag{24}$$

$$\frac{1}{m^*} = \frac{1}{m_k} + \frac{1}{m_l} \tag{25}$$

where ν_k, E_k and R_k denote the Poisson's ratio, Young's modulus and radius of solid particle k, respectively. The damping forces $\vec{F}_{d,\,kl}^{\,n}$ and $\vec{F}_{d,\,kl}^{\,t}$ are given by,

$$\vec{F}_{d,\,kl}^{\,n} = -2\sqrt{\frac{5}{6}}\psi\sqrt{\mathrm{C}_n\mathrm{m}^*\vec{v}_{\,kl}^{\,n}} \tag{26}$$

$$\vec{F}_{d,\,kl}^{\,t} = -2\sqrt{\frac{5}{6}}\psi\sqrt{\mathrm{C}_t\mathrm{m}^*\vec{v}_{\,kl}^{\,t}} \tag{27}$$

where $\vec{v}_{kl}^{\,n}$ and $\vec{v}_{kl}^{\,t}$ denote the relative velocity of contact point in normal and tangential directions between particle k and particle l. C_n and C_t denote the normal and tangential contact stiffness, defined by,

$$C_n = 2E^*\sqrt{R^*\left|\vec{\delta}_{kl}^{\,n}\right|} \tag{28}$$

$$C_t = 8G^*\sqrt{R^*\left|\vec{\delta}_{kl}^{\,n}\right|} \tag{29}$$

ψ is the damping ratio coefficient, given by,

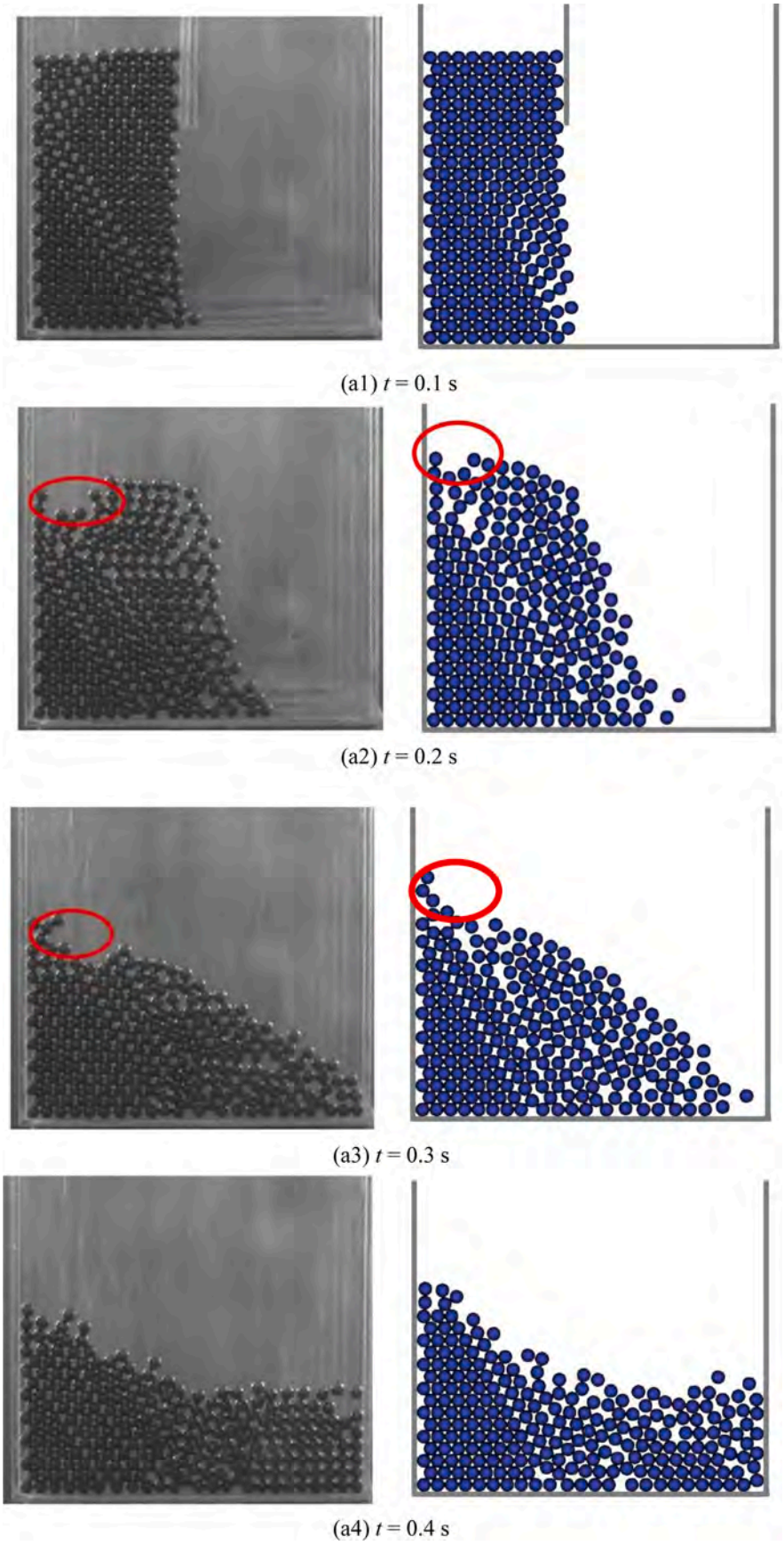

Fig. 6. Comparison in between the simulation snapshots by DEM and the experimental photos (Guo et al., 2017) - multilayer balls collapse.

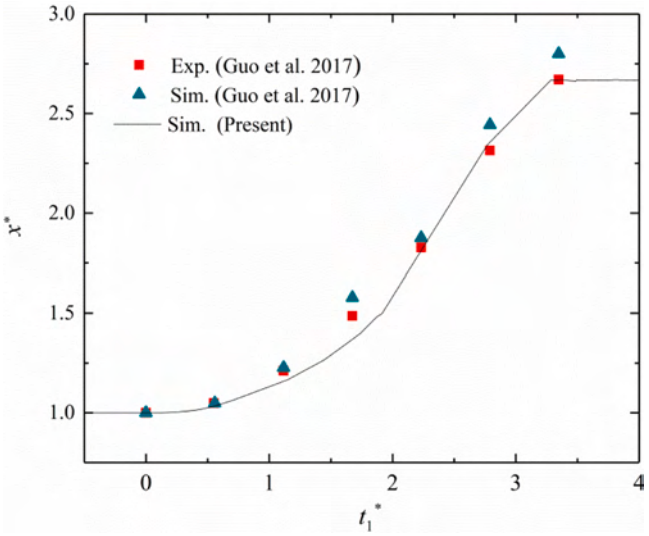

Fig. 7. Time histories of the leading front of balls in x direction - multilayer balls collapse.

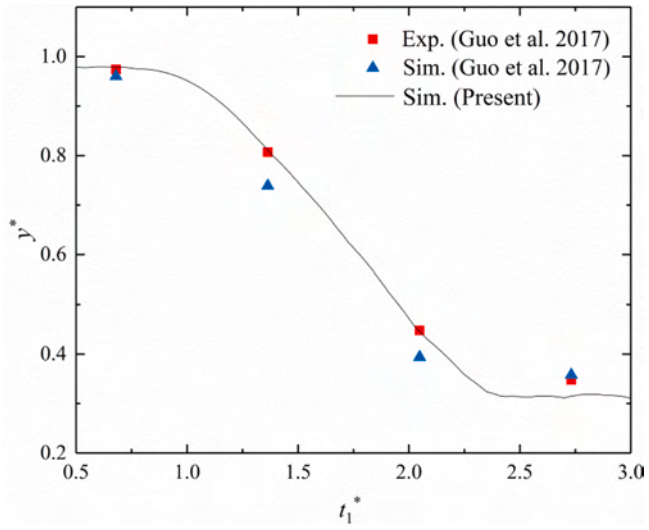

Fig. 8. Time histories of the vertical displacement of the ball at the upper-right corner of the layers - multilayer balls collapse.

Table 2
Parameters in the simulation of two-phase dam-break.

Solid phase	Values	Fluid phase	Values
Density (kg/m^3)	2500	Density (kg/m^3)	1000
Radius (m)	0.00135	Initial particle distance (m)	0.001
Young's modulus (N/m^2)	1.0×10^8	Kinematic viscosity (m^2/s)	1.0×10^{-6}
Poisson's ratio	0.2		
Static friction coefficient	0.2	-	-
Rolling friction coefficient	0.01	-	-
Coefficient of restitution	0.9	-	-
Time step(s)	1.0×10^{-6}	-	-

$$\psi = \ln(e)\Big/\sqrt{\ln^2(e)+\pi^2} \tag{30}$$

where e denotes restitution coefficient of solid particles. The total contact forces in normal direction can be calculated as,

$$\vec{F}^n_{c,\,kl} = \vec{F}^n_{e,\,kl} + \vec{F}^n_{d,\,kl} \tag{31}$$

The total contact forces in tangential direction are calculated according to whether particle i slides relative to particle j, given by,

$$\vec{F}^t_{c,\,kl} = \begin{cases} \vec{F}^t_{e,\,kl} + \vec{F}^t_{d,\,kl} & \left|\vec{F}^t_{c,\,kl}\right| < \mu_s\left|\vec{F}^n_{c,\,kl}\right| \\ -\mu_s\left|\vec{F}^n_{c,\,kl}\right|\dfrac{\vec{\delta}^t_{kl}}{\left|\vec{\delta}^t_{kl}\right|} & \left|\vec{F}^t_{c,\,kl}\right| > \mu_s\left|\vec{F}^n_{c,\,kl}\right| \end{cases} \tag{32}$$

where μ_s denotes the static friction coefficient.

The contact moment $\vec{T}_{c,\,kl}$ is composed of the moments arising from the tangential force $\vec{F}^t_{kl}$ and the torque $\vec{T}^r_{kl}$ (Zhou et al., 1999) due to the rolling friction, defined by,

$$\vec{T}^t_{kl} = \vec{F}^t_{c,\,kl} \times \vec{R}_k \tag{33}$$

$$\vec{T}^r_{kl} = -\mu_r R^* \left|\vec{F}^n_{kl}\right| \frac{\vec{\omega}_{kl}}{\left|\vec{\omega}_{kl}\right|} \tag{34}$$

where $\vec{\omega}_{kl}$ denotes the relative angular velocity, μ_r denotes the rolling friction coefficient.

2.3. Two-phase interaction

The hydrodynamic forces applied to DEM particles consist of drag force, pressure gradient force, virtual mass force and lubrication force. Because the drag force and pressure gradient force are dominant (Sakai et al., 2012) in the cases simulated by present study, the other hydrodynamic forces are ignored.

The drag force $\vec{F}^d_k$ acting on the solid particle is dependent on the local volume fraction and relative velocity between fluid and solid particle, given by,

$$\vec{F}^d_k = \frac{\beta_k}{1-\varepsilon_k}\left(\vec{u}_k - \vec{v}_k\right)V_k \tag{35}$$

where V_k denotes the volume of solid particle k. ε_k and $\vec{u}_k$ denote the local volume fraction and the fluid velocity in the center of solid particle k. Drag models of Ergun (Ergun, 1952) and Wen-Yu (Wen and Yu, 1966) are adopted and the interphase momentum exchange coefficient β_k is given by,

$$\beta_k = \begin{cases} 150\dfrac{(1-\varepsilon_k)^2}{\varepsilon_k}\dfrac{\mu_f}{d_k^2} + 1.75(1-\varepsilon_k)\dfrac{\rho_f}{d_k}\left|\vec{u}_k - \vec{v}_k\right| & \varepsilon_k \le 0.8 \\ 0.75C_d\dfrac{\varepsilon_k(1-\varepsilon_k)}{d_k}\rho_f\varepsilon_k^{-2.65}\left|\vec{u}_k - \vec{v}_k\right| & \varepsilon_k > 0.8 \end{cases} \tag{36}$$

where d_k denotes the diameter of the solid particle k. C_d denotes the drag coefficient, defined by,

$$C_d = \begin{cases} \dfrac{24}{\mathrm{Re}_k}\left(1+0.15\mathrm{Re}_k^{0.687}\right) & \mathrm{Re}_k \le 1000 \\ 0.44 & \mathrm{Re}_k > 1000 \end{cases} \tag{37}$$

The Reynolds number of solid particle k is defined as,

$$\mathrm{Re}_k = \frac{\varepsilon_k\rho_f d_k\left|\vec{u}_k - \vec{v}_k\right|}{\mu_f} \tag{38}$$

An extra weight function used to describe the solid-fluid interaction, which is proposed by Sun (Sun et al., 2014), written as,

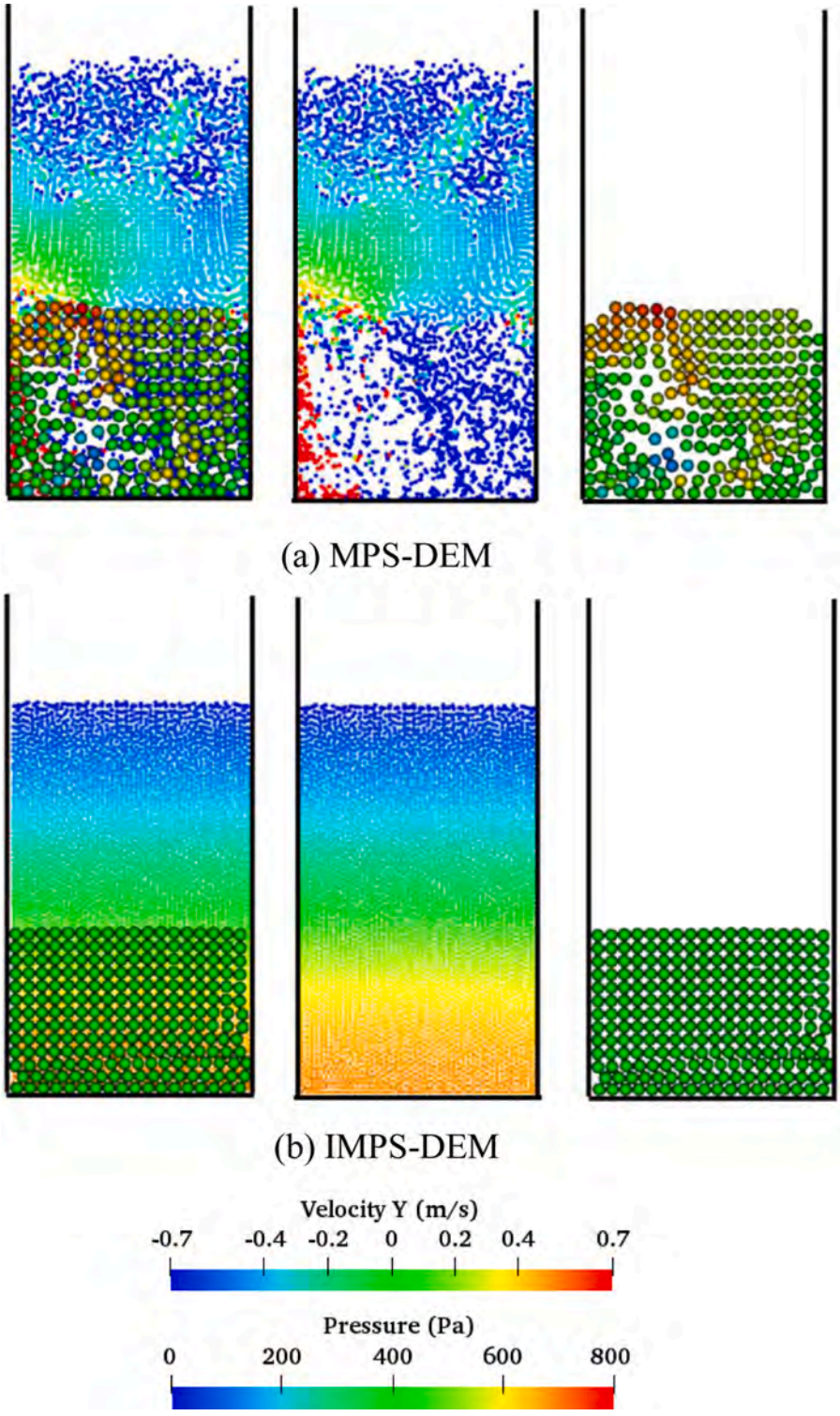

Fig. 9. Comparison in between the simulation snapshots by MPS-DEM and IMPS-DEM at t=0.07s - settling process.

$$W_s(r) = \begin{cases} 4(r/r_e)^5 - 5(r/r_e)^4 + 1 & r < r_e \\ 0 & r \geq r_e \end{cases} \tag{39}$$

The local volume fraction (Sun et al., 2014) of fluid particle i is calculated as,

$$\varepsilon_i = 1 - \frac{1}{\int W_s(|\vec{r}|)\mathrm{d}\vec{r}} \sum_k W_s\left(\left|\vec{r}_i - \vec{r}_k\right|\right) V_k \tag{40}$$

The local volume fraction and the fluid velocity (Sun et al., 2014) in the position of solid particle k are decided by neighboring fluid particles through the weight function W_s, given by,

$$\varepsilon_k = \frac{\sum_i \varepsilon_i W_s(|\vec{r}_i - \vec{r}_k|)}{\sum_i W_s\left(\left|\vec{r}_i - \vec{r}_k\right|\right)} \tag{41}$$

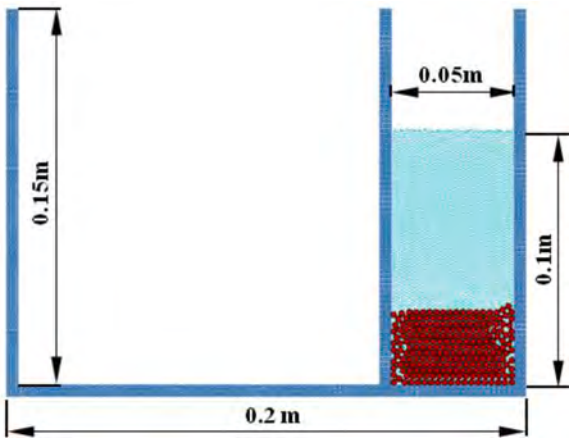

Fig. 10. Particles' distribution at $t = 0$s - two-phase dam-break.

$$\vec{u}_k = \frac{\sum_i \vec{u}_i W_s(|\vec{r}_i - \vec{r}_k|)}{\sum_i W_s\left(\left|\vec{r}_i - \vec{r}_k\right|\right)} \tag{42}$$

If the boundary particles of MPS are regarded as the neighbor particles of DEM, the fluid velocity at solid k may be affected by the wall velocity. Therefore, a new neighbor search strategy near the solid boundaries for solid-fluid particles is proposed, which refers to the neighbor particle search strategy near the free surface in Particle Shift Technology (PST) (Khayyer et al., 2017). The basic concept of this strategy is that the affect radius of solid-liquid will decrease and the boundary particles of MPS will be excluded from the neighbor list when the solid particles near the boundary, as shown in Fig. 2.

The drag force and the pressure gradient force can be combined (Feng and Yu, 2004) and the total hydrodynamic force exerted on the solid particles can be written as,

$$\vec{F}_k^{\text{int}} = \frac{\vec{F}_k^{d}}{\varepsilon_k} - V_k \rho_f \vec{g} \tag{43}$$

The reaction force acting on the fluid particles needs to satisfy the momentum conservation law, given by,

$$\vec{f}_i^{\text{int}} = \frac{1}{V_i} \sum_k \left(\vec{F}_k^{\text{int}} \frac{W_s(|\vec{r}_i - \vec{r}_k|)}{\sum_j W_s\left(\left|\vec{r}_j - \vec{r}_k\right|\right)} \right) \tag{44}$$

where V_i denotes the volume of fluid particle.

In some cases, some solid particles may rush out of the free surface and the hydrodynamics applied on those solid particles should be set to 0. A simple approach which is similar to the method of free surface detection is proposed to capture the solid particles which is out of the water, given by,

$$N_k < \gamma N_0 \tag{45}$$

where N_0 and N_i denote the initial number of neighboring fluid particles of solid particle k and the number of neighboring fluid particles of solid particle k. γ is set to 0.55 in this work.

2.4. Boundary condition

The boundaries for fluid particles and solid particles are treated separately as shown in Fig. 3. There are multilayer MPS particles arranged at the solid boundary. One layer of wall particles is arranged near the fluid particles and the pressures of wall particles are solved by PPE. Multilayer ghost particles are configured in order to provide support for fluid particles near the solid wall. The number of the layers is decided by

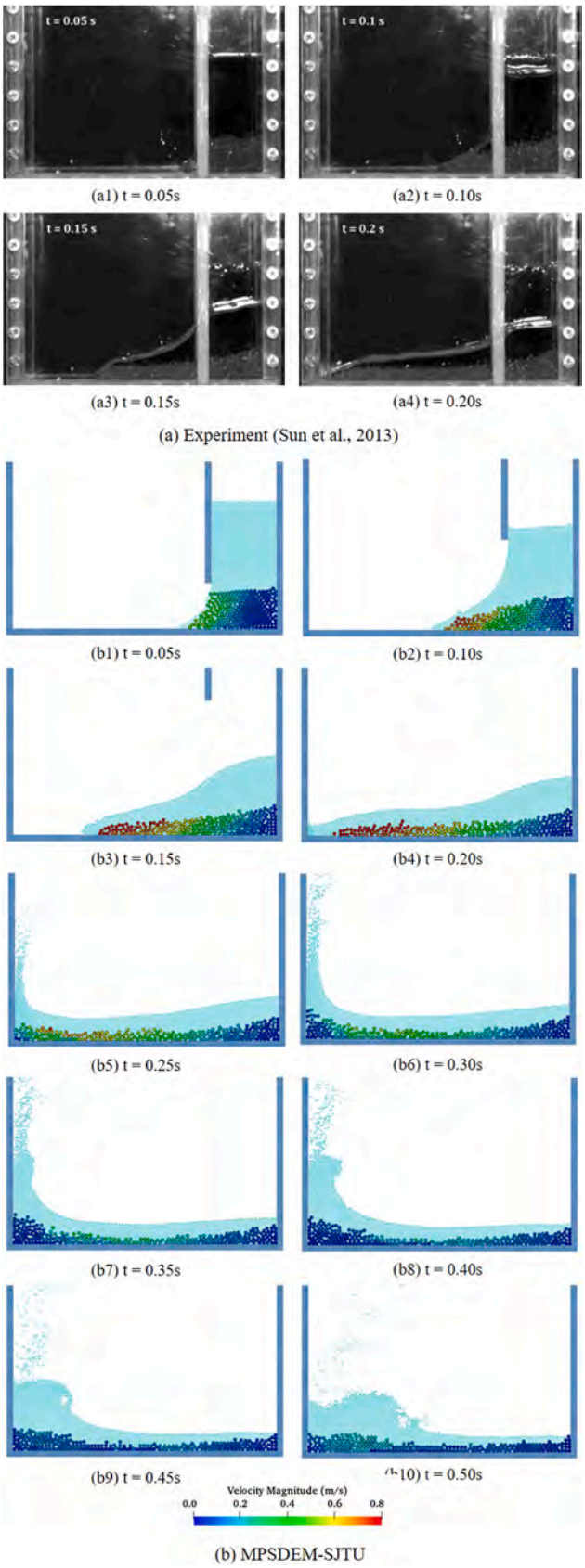

Fig. 11. Comparison in between the simulation snapshots by IMPS-DEM and experimental photos (Sun et al., 2013) - two-phase dam-break.

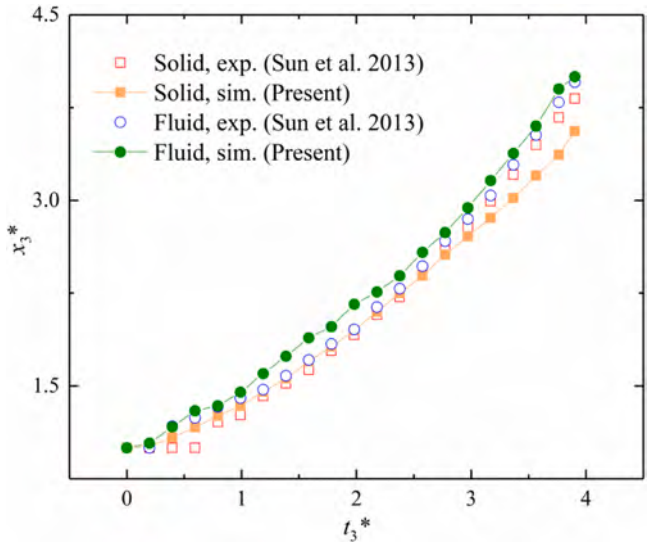

Fig. 12. Time histories of the leading front of liquid-solid flows - two-phase dam-break.

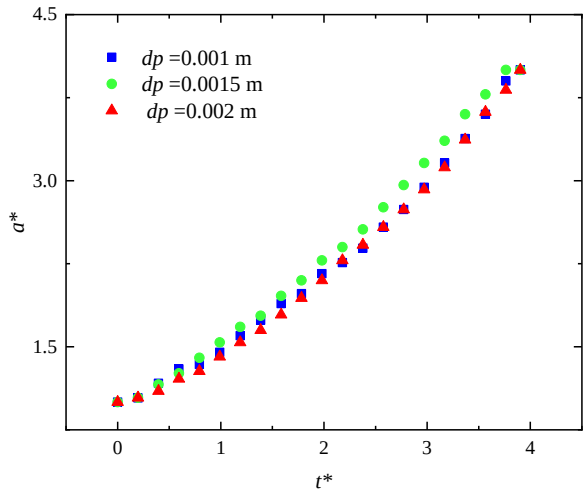

Fig. 13. Time histories of the leading front of the solid bed by IMPS-DEM with different MPS resolutions - two-phase dam-break.

the radius of particle interaction. The pressure of ghost particles is obtained by extrapolation. Both the wall particles and the ghost particles won't update their velocity and displacement after they gain the pressure. The line boundary for DEM solid particles is arranged to pass through all centers of MPS wall particles. The particle-wall collision can also be simulated with the Eqs. (20)-(34) and the wall can also be regarded as a soft sphere as the solid particles. The radius of the wall is decided by its curvature. The curvature and mass of the wall usually much larger than that of the solid particles and the Eqs. (23) and (25) can be reformulate as

$$\frac{1}{R_{kw}^*} = \frac{1}{R_k} \tag{46}$$

$$\frac{1}{m_{kw}^*} = \frac{1}{m_k} \tag{47}$$

where R_{kw}^* and m_{kw}^* are the equivalent radius and mass between the solid particles and the wall.

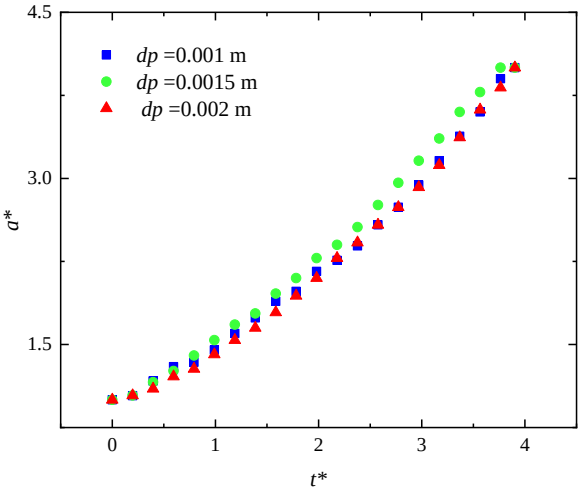

Fig. 14. Time histories of the leading front of the fluid by IMPS-DEM with different MPS resolutions - two-phase dam-break.

2.5. Time step

The incompressible MPS is a semi-implicit time-stepping method while DEM is an explicit time-stepping method. The time step for DEM simulation is usually much smaller than that for MPS simulation. For the stability of simulation, a relatively small time step is selected for MPS-DEM coupled method by previous study, which is time consuming. In present work, a multiple time-step algorithm is introduced for these two methods. The flow chart of coupling strategy between MPS and DEM is presented in Fig. 4 in detail.

The time step of MPS should satisfy Courant-Friedrichs-Lewy (CFL) condition, given by,

$$\frac{u_{f,\max}\Delta t_{\mathrm{mps}}}{\Delta l_0} < C \tag{48}$$

where $u_{f,\max}$, Δt_{mps}, Δl_0 and C donate the maximum velocity of fluid particles, the time step, the initial particle spacing and the courant number, respectively.

The time step of DEM is determined by (Thornton and Randall, 1988),

$$\Delta t_{\mathrm{dem}} < \frac{\pi R\sqrt{\rho/G}}{0.01631\nu + 0.8766} \tag{49}$$

In this work, the time step of MPS (Δt_{mps}) is set to 1×10^{-4} s while the time step of DEM is set to 1×10^{-6} s.

3. Numerical simulations

3.1. Validation of DEM model

In this section, the experiment of multilayer balls collapse conducted by Guo et al. (Guo et al., 2017) is employed to validate the DEM part of the MPSDEM-SJTU solver. Balls with 25 layers are initially arranged as a hexagonal packing scheme in a container as shown in Fig. 5. The solid balls are made of stainless steel and have a diameter of 0.01 m. The material of the container is PVC. The container has a length of 0.25 m and its width is equal to the ball diameter. There is a baffle near the right-most balls, which is 0.1 m from the left wall of the container. At the beginning of the experiment, the baffle moves upward at a constant speed of 1.4 m/s allowing balls to collapse under the action of gravity. The rest parameters of the simulation are presented in the Table 1. In order to make the system reach balance, solid particles have settled for 1.0 s before the baffle is removed. Therefore, the instant of removing the baffle is regarded as the starting point of the physical time.

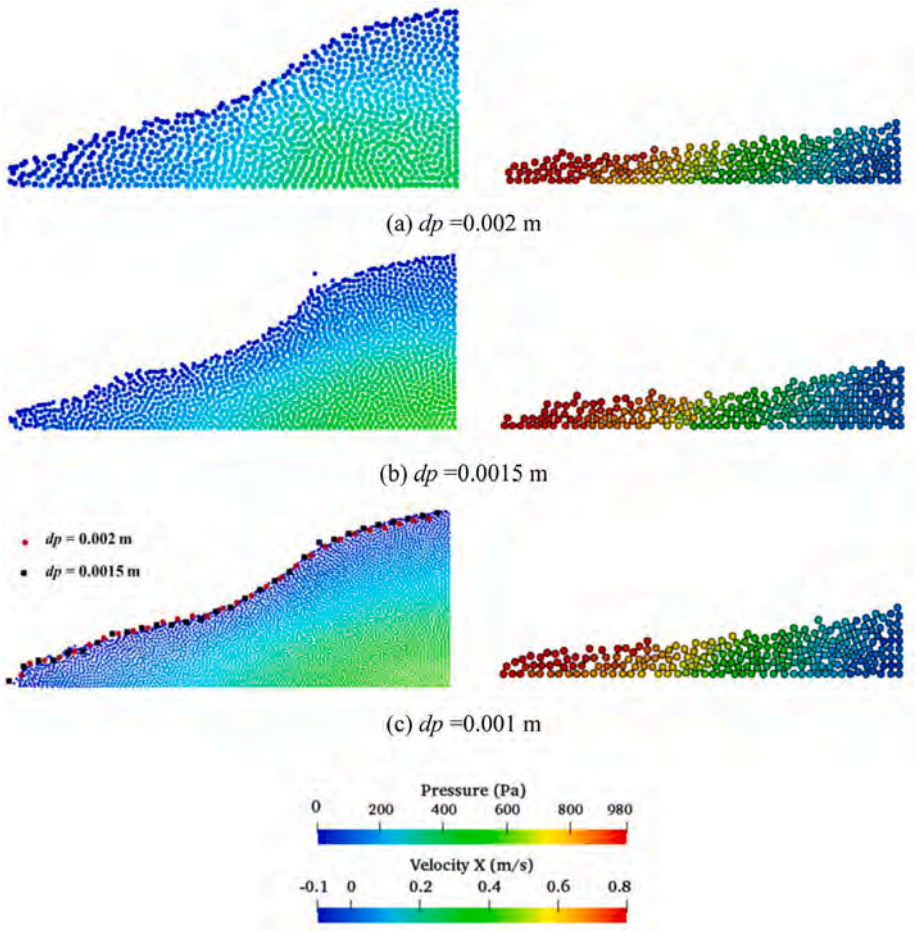

Fig. 15. Snapshots of the fluid phase and the solid bed by IMPS-DEM with different MPS resolutions at $t = 0.15$ s - two-phase dam-break.

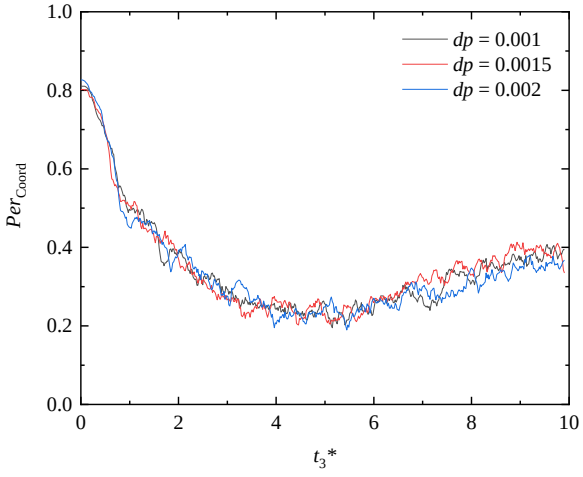

Fig. 16. Time histories of the aggregation degree of solid particles simulated by the IMPS-DEM with different MPS resolutions - two-phase dam-break.

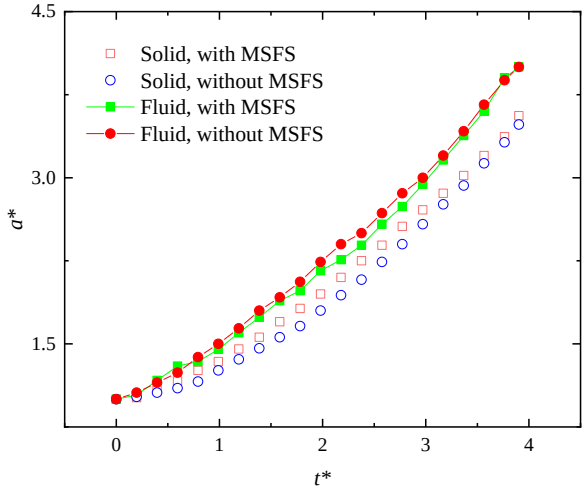

Fig. 17. Time histories of the leading front of liquid-solid flows simulated by the IMPS-DEM with MSFS and the IMPS-DEM without MSFS - two-phase dam-break.

The comparison of balls' distribution between the snapshots of the experiment and their counterparts of the simulation at different instants is shown in Fig. 6. Some typical phenomena can be observed in both experiment and simulation. It can be noticed that balls in the lower-left corner do not move obviously during the whole simulation. The gap observed in the upper-left corner will widen gradually and a slope will be formed in the end of the simulation.

Some dimensionless parameters are introduced to make a quantitative comparison of the solid particle movement.

$$x^* = x/l_1 \tag{50}$$

$$t_1^* = t_1\sqrt{g/l_1} \tag{51}$$

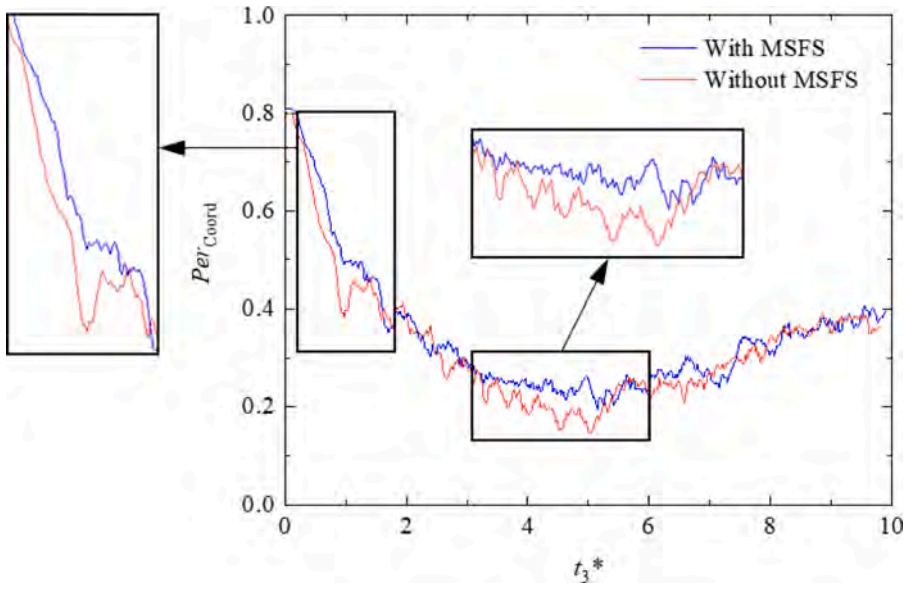

Fig. 18. Time histories of the aggregation degree of solid particles simulated by the IMPS-DEM with MSFS and the IMPS-DEM without MSFS - two-phase dam-break.

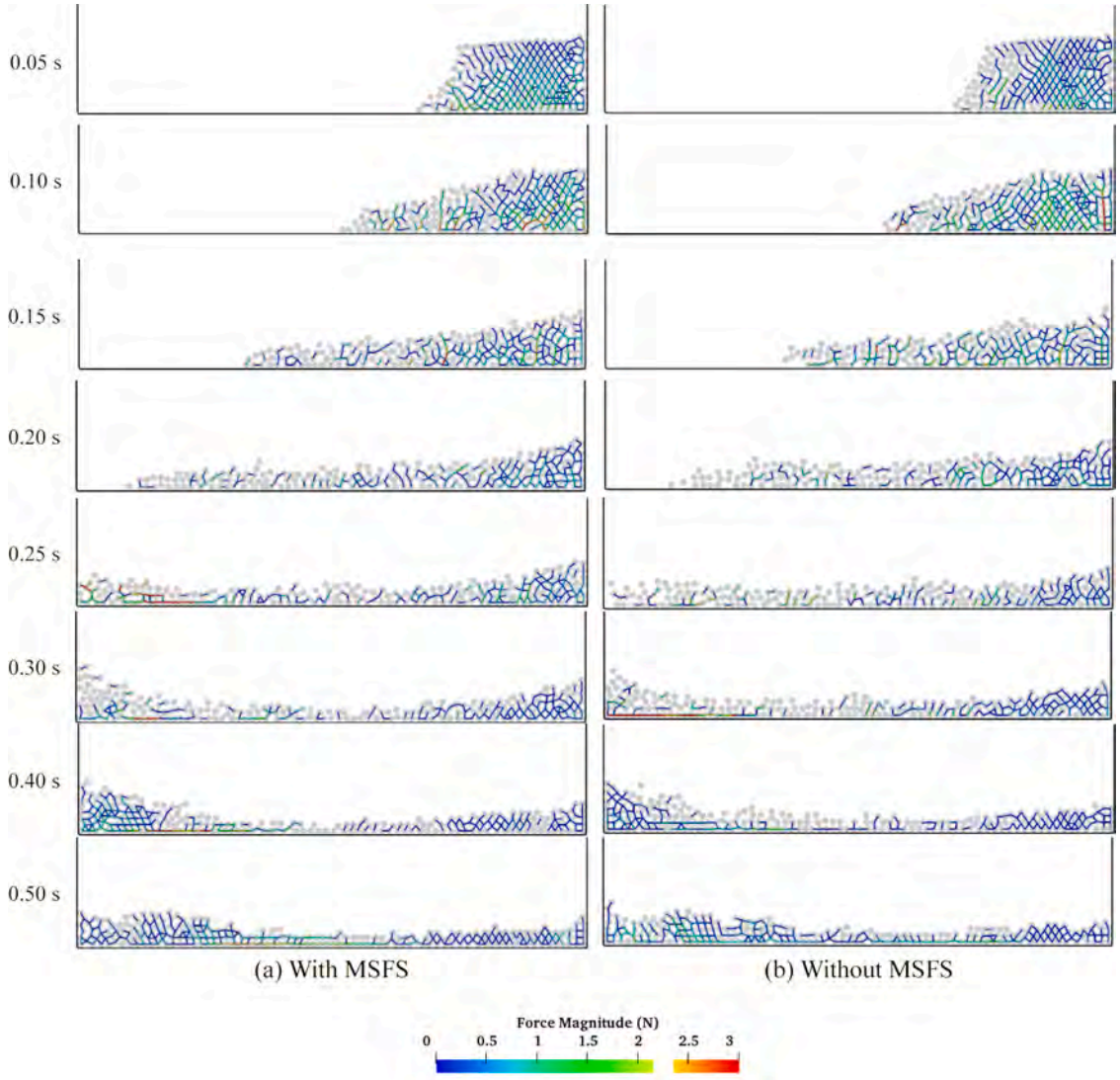

Fig. 19. Comparison between force chains' distribution of the IMPS-DEM with MSFS and the IMPS-DEM without MSFS - two-phase dam-break.

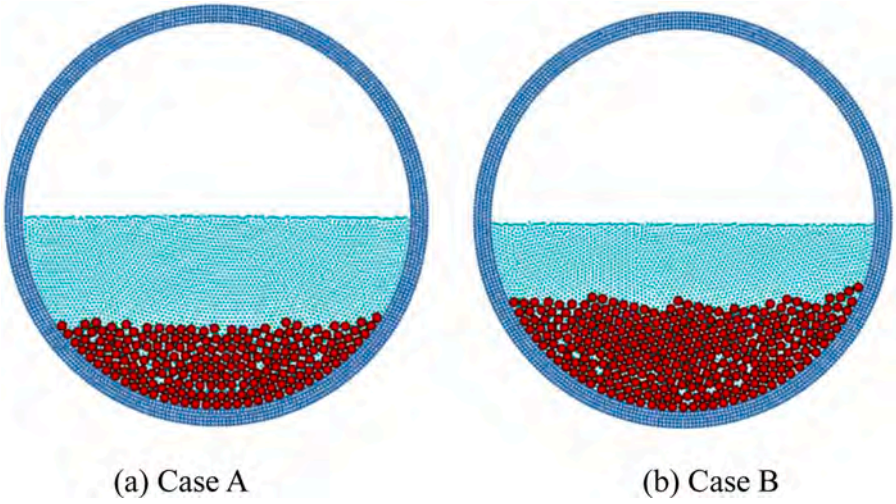

Fig. 20. Particles' distribution at $t = 0$s - two-phase flow in a rotating cylindrical tank.

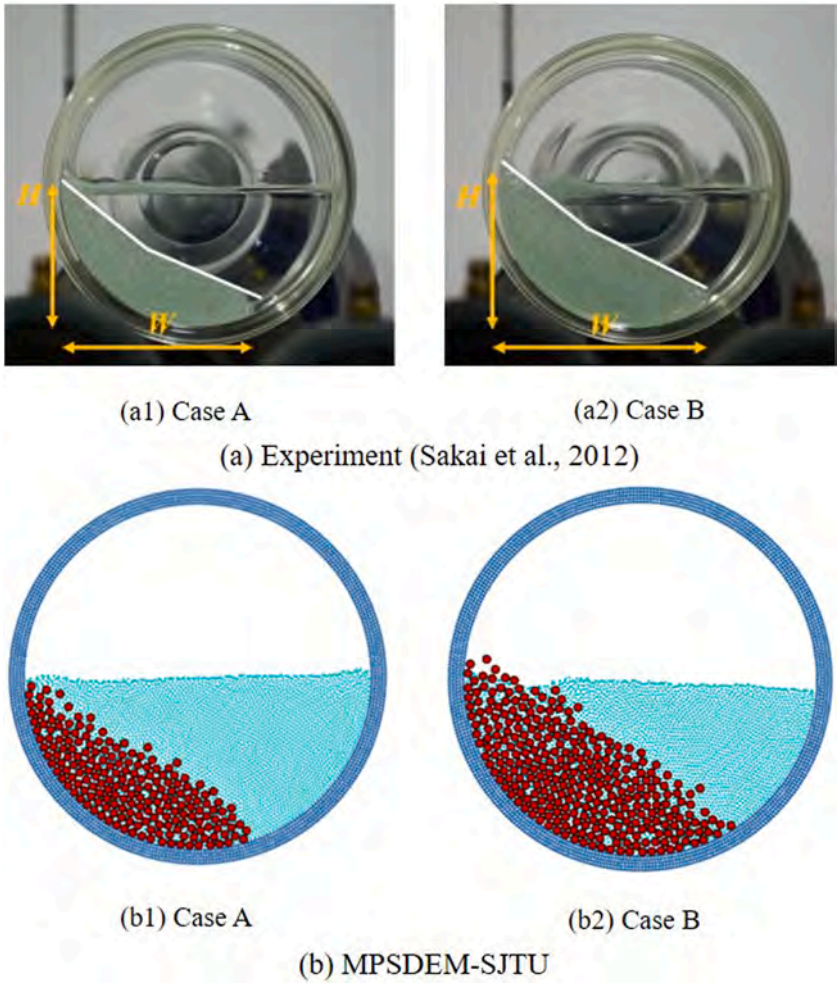

Fig. 21. Comparison in between the simulation snapshots by IMPS-DEM and experimental photos (Sakai et al., 2012) at the quasi-steady state - two-phase flow in a rotating cylindrical tank.

$$y^* = y/h \tag{52}$$

$$t_2^* = t_2\sqrt{g/h} \tag{53}$$

where x denotes the horizontal displacement of the particle front and t_1 is the corresponding physical time. y denotes the vertical displacement of the ball at the upper-right corner and t_2 is the corresponding physical time. l_1 denotes horizontal distance between left-most particles and right-most particles at the initial time. h denotes the height of the ball layers at the initial time.

Table 3
The height and the width of solid bed in the simulation of two-phase flow in a rotating cylindrical tank.

	Height (mm)	Error (%)	Width (mm)	Error (%)
Case A (Experiment (Sakai et al., 2012))	51.0	-	69.0	-
Case A (Simulation (Sakai et al., 2012))	54.1	6.1	72.9	5.7
Case A (Present study)	48.6	4.7	65.4	5.2
Case B (Experiment (Sakai et al., 2012))	60.5	-	77.8	-
Case B (Simulation (Sakai et al., 2012))	59.2	2.1	76.5	1.7
Case B (Present study)	57.0	5.9	77.6	0.3

As shown in the Figs. 7 and 8, the simulation results of present work are in good agreement with experimental results while the balls in the simulation of GUO et al. (Guo et al., 2017) move faster than that in the experiment. This is because that the movement of the baffle is taken into consideration in present work, which can slow down the balls. Overall, the DEM code developed in present study can simulate the solid-solid interaction correctly, which lays foundation for the further research on the coupling of MPS and DEM.

3.2. Two-phase dam-break

A simulation of two-phase dam-break is carried out and compared with experimental results of Sun et al. (Sun et al., 2013) to validate the accuracy of the MPSDEM-SJTU solver. The length of the tank is 0.2 m, while its height is 0.15 m. The solid bed is made of glass beads and the water is restricted to the right side of the tank by the gate which is 0.05 m from the right wall. Other parameters of the simulation can be founded in Table 2. The whole simulation can be divided into two processes: settling and dam-break.

Before the gate is removed, the tank rests until the state of the whole system reaches equilibrium. In this process, solid particles settle and squeeze the fluid particles out. The water level rises and reaches goal level (0.1 m). Fig. 9 shows the snapshoots of settling process at t=0.07s simulated by MPS-DEM and IMPS-DEM. In the MPS-DEM, the original MPS method proposed by Koshizuka (Koshizuka et al., 1995) is coupled with DEM. It can be noticed that the pressure obtained by MPS-DEM oscillates violently and the upward velocities of some DEM particles are extremely large, which leads to the termination of the simulation. On the contrary, the pressure field simulated by IMPS-DEM is smooth enough.

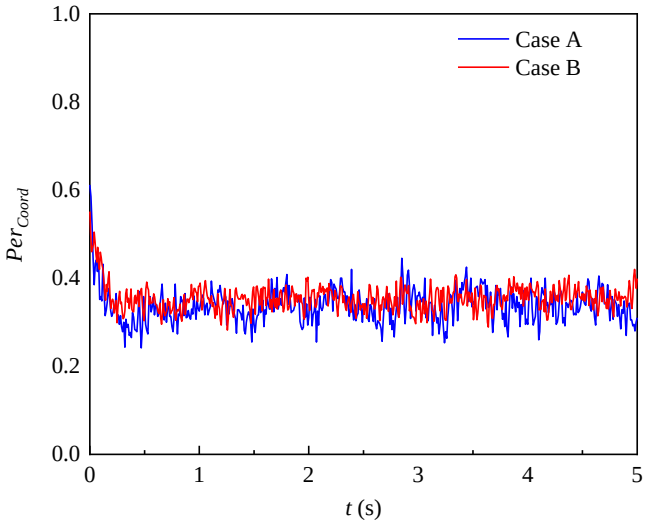

Fig. 23. Time histories of the aggregation degree of solid particles - two-phase flow in a rotating cylindrical tank.

After the settling process is finished, the simulation time for dam-break process is reset to 0. The numerical model at $t = 0$ s is shown in Fig. 10. In order to distinguish the fluid particles from the wall particles, the wall particles are displayed in a larger size. The gate moves upward at a constant speed of 0.68 m/s.

Fig. 11 shows a set of snapshots in the simulation of two-phase dam-break reproduced by IMPS-DEM in comparison with the experimental photos (Sun et al., 2013). The water and solid particles start to collapse under influence of gravity once the gate begins to move. Then, the fluid moves forward with the solid particles. According to the law of the energy conservation, part of the kinetic energy of fluid is converted into that of solid particles during the transport process. Before the front of solid bed reaches the left wall of the tank, it can be noted that the velocities of left-most solid particles are the highest. The front of the solid bed lags behind that of the water gradually in the simulation while the front of solid bed keeps the same pace with that of water in the experiment. Overall, the numerical results, such as the shapes of solid bed and free surface, agree well with experimental results. In order to describe

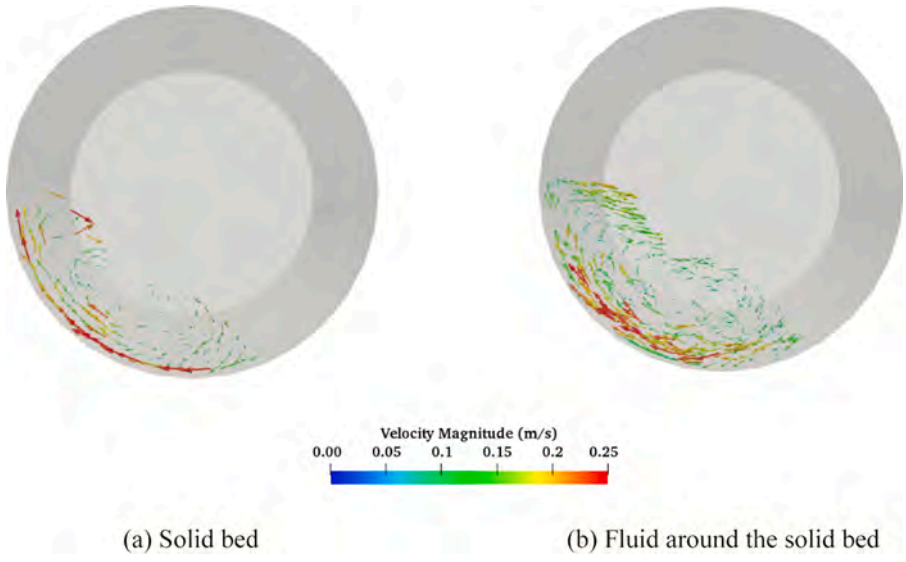

Fig. 22. Velocity vectors in liquid-solid field (Case A) - two-phase flow in a rotating cylindrical tank.

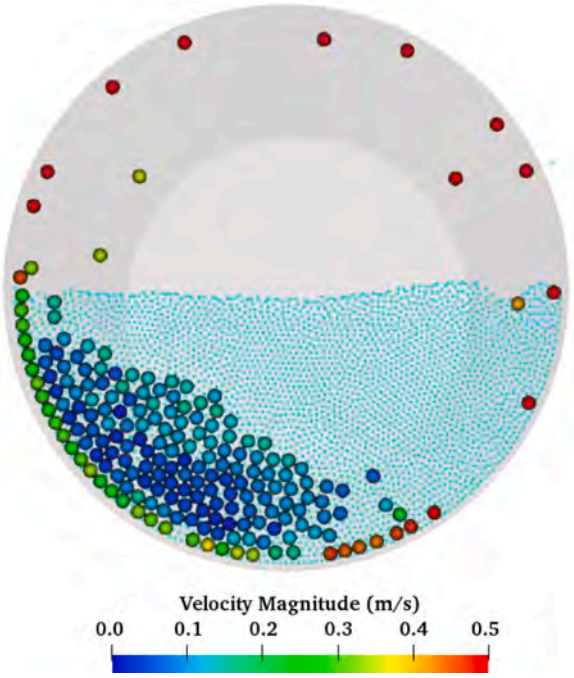

Fig. 24. Simulation snapshot simulated by the IMPS-DEM without MSFS (Case A) - two-phase flow in a rotating cylindrical tank.

the whole process of two-phase dam-break, more snapshots by the simulation of the MPSDEM-SJTU solver are presented. The water front arrives at the left wall at $t = 0.2$ s and solid particles almost cover the whole bottom of the tank. Then, the water climbs up along the left wall and solid particles follow the same motion. However, the rising height of solid particles is limited due to the action of gravity and they gather in the left corner of the tank. The water front reaches the highest position of the wall at t=0.3 s and an overturn of free surface is formed. Finally, the wave reflects from the left wall and provides rightward acceleration for some solid particles.

Fig. 12 shows the quantitative comparisons of the leading front of the solid-liquid flows between the numerical results reproduced by IMPS-DEM and the experimental data (Sun et al., 2013). Two dimensionless physical quantities are used here. The dimensionless position of the two-phase flow front and the dimensionless physical time are given by,

$$x_3^* = x_3/l_3 \tag{54}$$

$$t_3^* = t_3\sqrt{2g/l_2} \tag{55}$$

where x_3, l_3, t_3 and l_2 denote the front position of the liquid-solid flows, the length of the tank, the physical time and the distance between the gate and the right wall (0.05m), respectively. In the first half of the simulation, the front of solid bed coincides with the experimental result. However, during the latter half of the simulation, the front of solid bed lags behind that of experiment gradually. In the experiment, the velocity of fluid is almost the same as that of solid particles. In the simulation, the fluid moves noticeably faster than solid particles. There are many factors leading to these discrepancies. The main reason is that the numerical model is simplified to a 2-D model, while hydrodynamic forces acting on solid particles are not as accurate as the 3-D model. In addition, because the forces of virtual mass and lubrication are not considered in present study, the position of the front of the solid bed is underestimated. In general, the numerical results are in good agreement with the experimental results.

Additional simulations with initial MPS particle spacing (dp) being 0.0015 m and 0.002 m are also conducted to verify the convergency of present solver. Figs. 13 and 14 present the time histories of the leading front of the fluid phase and the solid bed with different MPS resolutions. It can be noticed that the numerical results with different MPS resolutions are almost consistent, showing the stability of present solver. Fig. 15 shows the snapshots of the fluid phase and solid bed by IMPS-DEM with different MPS resolutions at t = 0.15 s. Although the numerical results agree well with each other, it can be noted that the pressure field and the free surface of the numerical results with dp being 0.001 m is smoother than the others.

To further investigate the two-phase dam-break problem, the quantitative results are presented in Fig. 16. In this paper, a percentage number Per_{Coord} indicating the aggregation degree of solid particles is introduced, which is defined by,

$$Per_{\mathrm{Coord}} = Num_{\mathrm{Coord}}/N_{\max} = \left(2N_c \,/\, N_p\right)/N_{\max} \tag{56}$$

where Num_{Coord} is the coordination number representing the average number of contacts per DEM particles, derived from (Xu et al., 2019). $N_{\max}$ is the maximum contacts for each DEM particle with the same size, which is 6 in two-dimensional condition and 12 in three-dimensional condition. N_c and N_p denote the number of contacts and the number of particles.

Fig. 16 shows the time histories of aggregation degree of solid particles simulated by the IMPS-DEM with different MPS resolutions. It can be noticed that the curves of Per_{Coord} with different MPS resolutions follow the same trend. Per_{Coord} firstly decreases and then increases. Once the baffle is removed, Per_{Coord} drops sharply, which implies that the distribution of DEM particles becomes more scattered. The minimum point occurs when the solid bed reaches the right wall. With the solid particles gather in the right corner, Per_{Coord} increases gradually.

The new neighbor search strategy or Modified Solid-Fluid Search (MSFS) is tested in this case. Fig. 17 shows the comparison of the leading front of liquid-solid flows with MSFS and without MSFS. It can be noticed that the speed of the solid bed without MSFS is clearly slower than that with MSPS. The main reason is that the fluid velocity in the position of the bottom particle k is decreased by the bottom boundary whose velocity is zero.

Effects of MSFS to the internal structure evolution of the DEM particles are illustrated in Figs. 18 and 19. Force chain represents the line connecting two centers of two DEM particles in contact with each other. Once the gate is removed, the solid bed collapses immediately under the action of gravity and hydrodynamics. With the movement of the solid bed, the aggregation degree of the solid particles decreases and some force chains break quickly. It can be observed that the force chains tend to be sparse in the front of the solid bed. After the solid bed reaches the left wall, solid particles gather in the left corner of the tank and the force chains start to rebuild. It can be noticed that Per_{Coord} without MSFS drops more sharply than that with MSFS at the initial collapse stage, the similar phenomenon can also be observed at around $t = 0.05$ s in Fig. 19. The main reason is that the fluid velocities in the center of the bottom particles are underestimated if the MSFS is not adopted, which makes the particles move more slowly. the upper-left particles move forward faster and separate from the main body of the solid bed more easily. Besides, the rebuild of the force chains without MSFS is obviously slower than that with MSFS at the aggregation stage. This is because that the solid bed without MSFS lags behand that with MSFS. In general, the MSFS is necessary in this case.

3.3. Two-phase flow in a rotating cylindrical tank

In this subsection, a uniformly rotating cylindrical tank which is the same as the experimental model reported by Sakai et al. (Sakai et al., 2012) is selected as the numerical model. The diameter of the tank is 0.1 m and the depth of the water is 0.05 m. The tank rotates at 102 rpm. Fig. 20 shows the particles' distribution of the numerical model at $t = 0$s. Solid particles distribute randomly at the bottom of the tank and the surface of the solid bed is comparative flat. In Case A, the solid bed

consists of 200 particles. In Case B, the number of solid particles is 300. Other parameters are the same as those in the case of two-phase dam-break, as shown in Table 2.

In this case, the solid bed moves with the rotation of the tank, while the water prevents the movement of the solid particles. The whole system will reach a quasi-steady state after several seconds as shown in Fig. 21. In Case A, the shape of solid bed is bilinear in both simulation and experiment. However, in Case B, the bilinear shape of solid bed observed in simulation is not as obvious as that in experiment. The height and the width of solid bed in simulations are compared with experimental results, which are presented in Table 3. In Case A, the solid bed simulated by Sakai et al. (Sakai et al., 2012) covers a wider range than the results of experiment and present study. In Case B, the height of solid bed simulated by Sakai et al. (Sakai et al., 2012) is closer to the experimental results compared with the present study. Different contact models adopted by Sakai et al. (Sakai et al., 2012) and present study may lead to these discrepancies. In general, results of present study are in good agreement with experimental results, which shows that the MPSDEM-SJTU solver has the ability to deal with the problems of liquid-solid flows with moving boundary.

Fig. 22 shows the velocity vectors in the liquid-solid field in Case A. Velocity in magnitude is largest near the moving boundary in both solid and fluid field. The velocities of the solid particles inside the solid bed are relatively small and their directions are more random. Besides, it is obviously that the velocity of solid is related to the velocity of the fluid around the solid bed in both magnitude and direction.

Time histories of the aggregation degree of solid particles are shown in Fig. 23. It can be seen that Per_{Coord} drops sharply firstly and then reaches a quasi-state. Those two curves oscillate violently, which mainly results from the small number of DEM particles used in the simulations. If those cases are extended to three-dimensional condition, the curves may be smoother. It can also be noted that the values of Per_{Coord} in the cases with different numbers of particles are close to each other the when the whole system at the quasi-state, which implies that the aggregation degree will not increase when the quantity of particles is large enough.

This case is also simulated by the IMPS-DEM without MSFS. Fig. 24 shows the snapshot simulated by the IMPS-DEM without MSFS in Case A. It can be noted that some solid particles with high-speed climb up the wall of cylinder after they rush out of the water, which is different from that observed in experiment and the simulation with MSFS. The DEM particles which is close to the moving boundary are speeded up by the boundary particles of MPS. It can also be concluded that the fluid velocities in the center of the solid particles, which are close to the moving boundary, should be modified with MSFS.

4. Conclusions

In this work, an in-house solver MPSDEM-SJTU is developed for the simulation of liquid-solid two-phase flows. The IMPS module is applied for fluid flow simulation while the DEM module is used to trace the movements of solid particles. The interaction between the fluid phase and the solid phase is based on the local average technique. A coupled strategy with different boundary treatments and multiple time steps for fluid and solid particles is introduced. The free-surface detection and the solid-fluid neighbor search are also modified.

The simulation of multilayer balls collapse is conducted to validate the DEM code firstly. Compared with other simulations, the movement of the gate is considered in present work, which improves the accuracy of calculation. Secondly, two-phase dam-break flows with different MPS multi-resolutions are simulated and compared with experimental results to check the accuracy and convergency of present solver. Numerical results by MPS-DEM and IMPS-DEM model in settling process are compared. The pressure field of fluid phase is smoother and the velocity field in solid phase is more stable in the results by IMPS-DEM. Finally, a moving boundary case, the liquid-solid flows in a rotating cylindrical tank is simulated. The whole system will reach a quasi-steady state and the height and width of solid bed in simulations are close to those in experiments. The Modified Solid-Fluid Search (MSFS) can effectively decrease the influence of solid boundary. Overall, the MPSDEM-SJTU solver has the ability to simulate the liquid-solid flows with free surface.

In fact, 3-D flows are more complicated and the 3-D effect cannot be ignored. In previous work (Chen and Wan, 2019, Xie et al., 2020), the solver for 3-D single phase flow has been developed with GPU acceleration technique, which can improve the calculation efficiency. In the future, the solver for 3-D liquid-solid flows will be developed based on the GPU platform and applied for solving the complex problems of coastal and ocean engineering.

Declaration of Competing Interest

The authors declare that they have no known competing financial interests or personal relationships that could have appeared to influence the work reported in this paper.

Acknowledgements

This work is supported by the National Key Research and Development Program of China (2019YFB1704200 and 2019YFC0312400), National Natural Science Foundation of China (51879159), to which the authors are most grateful.

References

Harada, E., Gotoh, H., Ikari, H., Khayyer, A., 2019. Numerical simulation for sediment transport using MPS-DEM coupling model. Adv. Water Resour. 129, 354–364.
Hutter, K., Svendsen, B., Rickenmann, D., 1996. Debris flow modeling: a review. Continuum Mech. Thermodyn. 8 (1), 1–35.
Markauskas, D., Kruggel-Emden, H., Scherer, V., 2018. Numerical analysis of wet plastic particle separation using a coupled DEM-SPH method. Powder Technol 325, 218–227.
Winardi, S., Widiyastuti, W., Septiani, E.L., Nurtono, T., 2018. Simulation of solid-liquid flows in a stirred bead mill based on computational fluid dynamics (CFD). Mater. Res. Express 5 (5).
Gingold, R.A., Monaghan, J.J., 1977. Smoothed particle hydrodynamics: theory and application to non-spherical stars. Mon. Not. Roy. Astron. Soc. 181 (3), 375–389.
Shao, S., Lo, E.Y.M., 2003. Incompressible SPH method for simulating Newtonian and non-Newtonian flows with a free surface. Adv. Water Resour. 26, 787–800.
Koshizuka, S., Oka, Y., Tamako, H., 1995. A particle method for calculating splashing of incompressible viscous fluid. Int. Conf. Math. Comput. Reactor. Phys. Environ. Anal. 2, 1514–1521.
Cundall, P.A., Strack, O.D.L., 1979. A discrete numerical model for granular assembles. Geotechnique 29, 47–65.
Gotoh, H., Khayyer, A., 2018. On the state-of-the-art of particle methods for coastal and ocean engineering. Coastal Engineering Journal 60 (1), 79–103.
Zhang, X.S., Wang, J.H., Wan, D.C., 2020. Numerical techniques for coupling hydrodynamic problems in ship and ocean engineering. J. Hydrodyn. 32 (4), 212–233.
Zhu, Y., Zhang, C., Yu, Y., Hu, X., 2021. A CAD-compatible body-fitted particle generator for arbitrarily complex geometry and its application to wave-structure interaction. J. Hydrodyn. 33 (2), 195–206.
Khayyer, A., Gotoh, H., Falahaty, H., Shimizu, Y., 2018. Towards development of enhanced fully-lagrangian mesh-free computational methods for fluid-structure interaction. J. Hydrodyn. 30 (1), 49–61.
Shimizu, Y., Khayyer, A, Gotoh, H, Nagashima, K, 2020. An enhanced multiphase ISPH-based method for accurate modeling of oil spill. Coastal Engineering Journal 62 (4), 625–646.
Tsurudome, C., Liang, D., Shimizu, Y., Khayyer, A., Gotoh, H., 2020. Incompressible SPH simulation of solitary wave propagation on permeable beaches. J. Hydrodyn. 32 (4), 664–671.
Tsuruta, N., Gotoh, H., Suzuki, K., Ikari, H., Shimosako, K., 2019. Development of PARISPHERE as the particle-based numerical wave flume for coastal engineering problems. Coast. Eng. J. 61 (1), 41–62.
Ikari, H., Yamano, T., Gotoh, H., 2020. Multiphase particle method using an elastoplastic solid phase model for the diffusion of dumped sand from a split hopper. Comput. Fluids 208, 104639.
Tajnesaie, M., Shakibaeinia b, A., Hosseini, K., 2018. Meshfree particle numerical modelling of sub-aerial and submerged landslides. Comput. Fluids 172, 109–121.
Khanpour, M., Zarrati, A.R., Kolahdoozan, M., Shakibaeinia, A., Amirshahi, S.M., 2016. Mesh-free SPH modeling of sediment scouring and flushing. Comput. Fluids 129, 67–78.
Feng, Y.Q., Yu, A.B., 2004. Assessment of Model Formulations in the Discrete Particle Simulation of Gas-Solid Flow. Ind. Eng. Chem. Res. 43 (26), 8378–8390.

Xiong, Q.G., Deng, L.J., Wang, W., Ge, W., 2011. SPH method for two-fluid modeling of particle-fluid fluidization. Chem. Eng. Sci. 66, 1859–1865.
Tajnesaie, M., Shakibaeinia, A., Hosseini, K., 2021. Enhanced weakly-compressible MPS method for immersed granular flows. Adv. Water Resour. 152, 103908.
Tan, H., Chen, S., 2017. A hybrid DEM-SPH model for deformable landslide and its generated surge waves. Adv. Water Resour. 108, 256–276.
Pantaleev, S., Yordanova, S., Janda, A., Marigo, M., Ooi, J.Y., 2017. An experimentally validated DEM study of powder mixing in a paddle blade mixer. Powder Technol 311, 287–302.
González-Montellano, C., Ramírez, á., Gallego, E., Ayuga, F., 2011. Validation and experimental calibration of 3D discrete element models for the simulation of the discharge flow in silos. Chem. Eng. Sci. 66 (21), 5116–5126.
Zhang, S., Kuwabara, S., Suzuki, T., Kawano, Y., Morita, K., Fukuda, K., 2009. Simulation of solid-fluid mixture flow using moving particle methods. J. Comput. Phys. 228, 2552–2565.
Anderson, T.B., Jackson, R., 1969. Fluid Mechanical Fluid mechanical description of fluidized beds. Comparison of theory and experiment. Ind. Eng. Chem. Fundamen 6 (4), 137–144.
Robinson, M.J., Luding, S., Ramaioli, M., 2014. Fluid-particle flow simulations using two-way-coupled mesoscale SPH-DEM and validation. Int. J. Multiph. Flow 59 (2), 121–134.
Sun, X., Sakai, M., Sakai, M.T., Yamada, Y., 2014. A Lagrangian-Lagrangian coupled method for three-dimensional solid-liquid flows involving free surfaces in a rotating cylindrical tank. Chem. Eng. J. 246, 122–141.
Sun, X., Sakai, M., Yamadaa, Y., 2013. Three-dimensional simulation of a solid-liquid flow by the DEM-SPH method. J. Comput. Phys. 248, 147–176.
He, Y., Bayly, A.E., Hassanpour, A., Muller, F., Wu, K., Yang, D.M., 2018. A GPU-based coupled SPH-DEM method for particle-fluid flow with free surfaces. Powder Technol 338, 548–562.
Iwamoto, T., Nakase, H., Nishiura, D., Sakaguchi, H., Miyamoto, J., Tsurugasaki, K., Kiyono, J., 2019. Application of SPH-DEM coupled method to failure simulation of a caisson type composite breakwater during a tsunami. Soil Dyn. Earthq. Eng. 127, 105806.
Markauskas, D., Kruggel-Emden, H., 2019. Coupled DEM-SPH simulations of wet continuous screening. Adv. Powder Technol 30 (12), 2997–3009.
Li, J.J., Qiu, L.C., Tian, L., Yang, Y.S., Han, Y., 2019. Modeling 3D non-newtonian solid-liquid flows with a free-surface using DEM-MPS. Eng. Anal. Bound. Elem. 105, 70–77.
Xu, W.J., Dong, X.Y., 2021. Simulation and verification of landslide tsunamis using a 3D SPH-DEM coupling method. Comput. Geotech. 129, 103803.
Sakai, M., Shigeto, Y., Sun, X., Aoki, T., Saito, T., Xiong, J., Koshizuka, S., 2012. Lagrangian-lagrangian modeling for a solid–liquid flow in a cylindrical tank. Chem. Eng. J. 200-202, 663–672.
Luo, M., Khayyer, A., Lin, P.Z., 2021. Particle methods in ocean and coastal engineering. App. Ocean Res.
Tanaka, M., Masunaga, T., 2010. Stabilization and smoothing of pressure in MPS method by quasi-compressibility. J. Comput. Phys. 229 (11), 4279–4290.
Khayyer, A., Gotoh, H., 2010. A higher order Laplacian model for enhancement and stabilization of pressure calculation by the MPS method. App. Ocean Res. 32 (1), 124–131.
Khayyer, A., Gotoh, H., 2012. A 3D higher order Laplacian model for enhancement and stabilization of pressure calculation in 3D MPS-based simulations. Appl. Ocean Res 37, 120–126.
Khayyer, A., Gotoh, H., 2011. Enhancement of stability and accuracy of the moving particle semi-implicit method. J. Comput. Phys. 230 (8), 3093–3118.
Khayyer, A., Gotoh, H., 2009. Modified Moving Particle Semi-implicit methods for the prediction of 2D wave impact pressure. Coast. Eng. 56 (4), 419–440.
Khayyer, A., Gotoh, H., Falahaty, H., Shimizu, Y., 2018. An enhanced ISPH-SPH coupled method for simulation of incompressible fluid-elastic structure interactions. Comput. Phys. Commun. 232, 139–164.
Khayyer, A., Tsuruta, N., Shimizu, Y., Gotoh, H., 2018. Multi-resolution MPS for incompressible fluid-elastic structure interactions in ocean engineering. App. Ocean Res. 82, 397–414.
Khayyer, A., Tsuruta, N., Shimizu, Y., Gotoh, H., 2021. Multi-resolution ISPH-SPH for accurate and efficient simulation of hydroelastic fluid-structure interactions in ocean engineering. Ocean Eng. 226, 108652.
Khayyer, A., Shimizu, Y., Gotoh, H., Nagashima, K., 2021. A coupled incompressible SPH-Hamiltonian SPH solver for hydroelastic FSI corresponding to composite structures. Appl. Mathem. Model. 94 (1).
Khayyer, A., Gotoh, H., Shimizu, Y., 2019. A projection-based particle method with optimized particle shifting for multiphase flows with large density ratios and discontinuous density fields. Comput. Fluids 179, 356–371.
Wang, L., Khayyer, A., Gotoh, H., Jiang, Q., Zhang, C., 2019. Enhancement of pressure calculation in projection-based particle methods by incorporation of background mesh scheme. App. Ocean Res. 86, 320–339.
Zhang, Y.L., Wan, D.C., 2017. Numerical study of interactions between waves and free rolling body by IMPS method. Comput. Fluids 155, 124–133.
Kafui, K.D., Thornton, C., Adams, M.J., 2002. Discrete particle-continuum fluid modelling for gas–solid fluidized beds. Chem. Eng. Sci. 57 (13), 2395–2410.
Zhang, Y.X., Wan, D.C., Hino, T., 2014. Comparative study of MPS method and level-set method for sloshing flows. J. Hydrodyn. 26 (4), 577–585.
Khayyer, A., Gotoh, H., Shao, S., 2009. Enhanced predictions of wave impact pressure by improved incompressible SPH methods. App. Ocean Res. 31 (2), 111–131.
Hertz, H., 1881. Ueber die Berührung fester elastischer Koerper. J. Reine Angew. Math. 92, 156–171.
Mindlin, R.D., 1949. Compliance of elastic bodies in contact. ASME Trans. J. Appl. Mech. 16, 259–268.
Zhou, Y.C., Wright, B.D., Yang, R.Y., Xu, B.H., Yu, A.B., 1999. Rolling friction in the dynamic simulation of sandpile formation. Phys. A 269, 536–553.
Ergun, S., 1952. Fluid flow through packed columns. Chem. Eng. Prog. 48, 89–94.
Wen, C., Yu, Y., 1966. Mechanics of fluidization. Chem. Eng. Progress Symposium Series 62, 100–111.
Khayyer, A., Gotoh, H., Shimizu, Y., 2017. Comparative study on accuracy and conservation properties of two particle regularization schemes and proposal of an optimized particle shifting scheme in ISPH context. J. Comput. Phys. 332, 236–256.
Thornton, C., Randall, C.W., 1988. Applications of theoretical contact mechanics to solid particle system simulation. In: Satake, M, Jenkins, TJ (Eds.), Micromechanics Granular matters. Elsevier, Amsterdam, pp. 133–142.
Guo, K., Chen, R., Li, Y., Qiu, S., Su, G.H., 2017. Numerical investigation of the fluid-solid mixture flow using the FOCUS code. Prog. Nucl. Energy 97, 197–213.
Xu, W.J., Dong, X.Y., Ding, W.T., 2019. Analysis of fluid-particle interaction in granular materials using coupled sph-dem method. Powder Technol. 353, 459–472.
Chen, X., Wan, D.C., 2019. GPU accelerated MPS method for large-scale 3-D violent free surface flows. Ocean Eng. 171, 677–694.
Xie, F.Z., Zhao, W.W., Wan, D.C., 2020. CFD simulations of three-dimensional violent sloshing flows in tanks based on MPS and GPU. J. Hydrodyn. 32 (4), 672–683.